JACS
JOURNAL OF THE AMERICAN CHEMICAL SOCIETY
pubs.acs.org/JACS

Article

Structure–Toxicity Relationship in Intermediate Fibrils from α-Synuclein Condensates

Serene W. Chen,♦ Joseph D. Barritt,♦ Roberta Cascella, Alessandra Bigi, Cristina Cecchi, Martina Banchelli, Angelo Gallo, James A. Jarvis, Fabrizio Chiti, Christopher M. Dobson, Giuliana Fusco,* and Alfonso De Simone*

Cite This: J. Am. Chem. Soc. 2024, 146, 10537–10549

Read Online

ACCESS | Metrics & More | Article Recommendations | Supporting Information

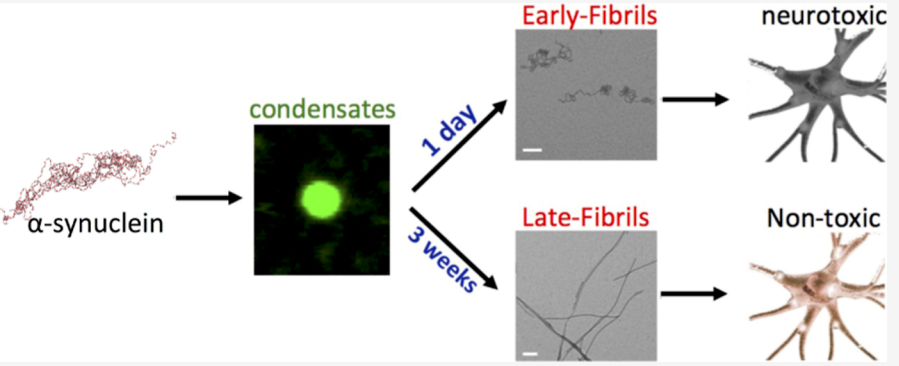

ABSTRACT: The aberrant aggregation of α-synuclein (αS) into amyloid fibrils is associated with a range of highly debilitating neurodegenerative conditions, including Parkinson's disease. Although the structural properties of mature amyloids of αS are currently understood, the nature of transient protofilaments and fibrils that appear during αS aggregation remains elusive. Using solid-state nuclear magnetic resonance (ssNMR), cryogenic electron microscopy (cryo-EM), and biophysical methods, we here characterized intermediate amyloid fibrils of αS forming during the aggregation from liquid-like spherical condensates to mature amyloids adopting the structure of pathologically observed aggregates. These transient amyloid intermediates, which induce significant levels of cytotoxicity when incubated with neuronal cells, were found to be stabilized by a small core in an antiparallel β-sheet conformation, with a disordered N-terminal region of the protein remaining available to mediate membrane binding. In contrast, mature amyloids that subsequently appear during the aggregation showed different structural and biological properties, including low levels of cytotoxicity, a rearranged structured core embedding also the N-terminal region, and a reduced propensity to interact with the membrane. The characterization of these two fibrillar forms of αS, and the use of antibodies and designed mutants, enabled us to clarify the role of critical structural elements endowing intermediate amyloid species with the ability to interact with membranes and induce cytotoxicity.

INTRODUCTION

α-Synuclein (αS) is an intrinsically disordered protein whose aggregation is strongly associated with synucleinopathies, a group of neurodegenerative disorders that includes Parkinson's disease (PD).[1−7] These pathologies afflict more than 2% of the global population over the age of 65, and their prevalence is expected to increase significantly with increasing life expectancy. In its physiological form, αS has been shown to localize predominantly at the presynaptic termini.[8] The function of αS is currently unknown; however, evidence exists about some possible roles in neuronal physiological processes such as the regulation of the exocytosis of synaptic vesicles (SVs),[9−12] vesicular trafficking,[13,14] and mitochondrial binding.[15,16] In the context of PD, amyloid aggregates of αS result in the major constituents of Lewy bodies, intracellular inclusions, forming in dopaminergic neurons of patients.[2,17,18] In addition, familial forms of early-onset PD have been linked with genetic alterations in patients, including mutations, duplications, and triplications of the αS encoding gene (SNCA).[19,20] The structural properties of amyloid fibrils of αS have been extensively studied,[21−26] including fibrils formed in vitro by WT αS and pathological mutants[27,28] as well as post-mortem aggregates purified from the brains of patients affected by

Received: December 26, 2023
Revised: March 14, 2024
Accepted: March 15, 2024
Published: April 3, 2024

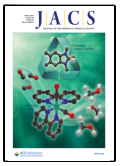

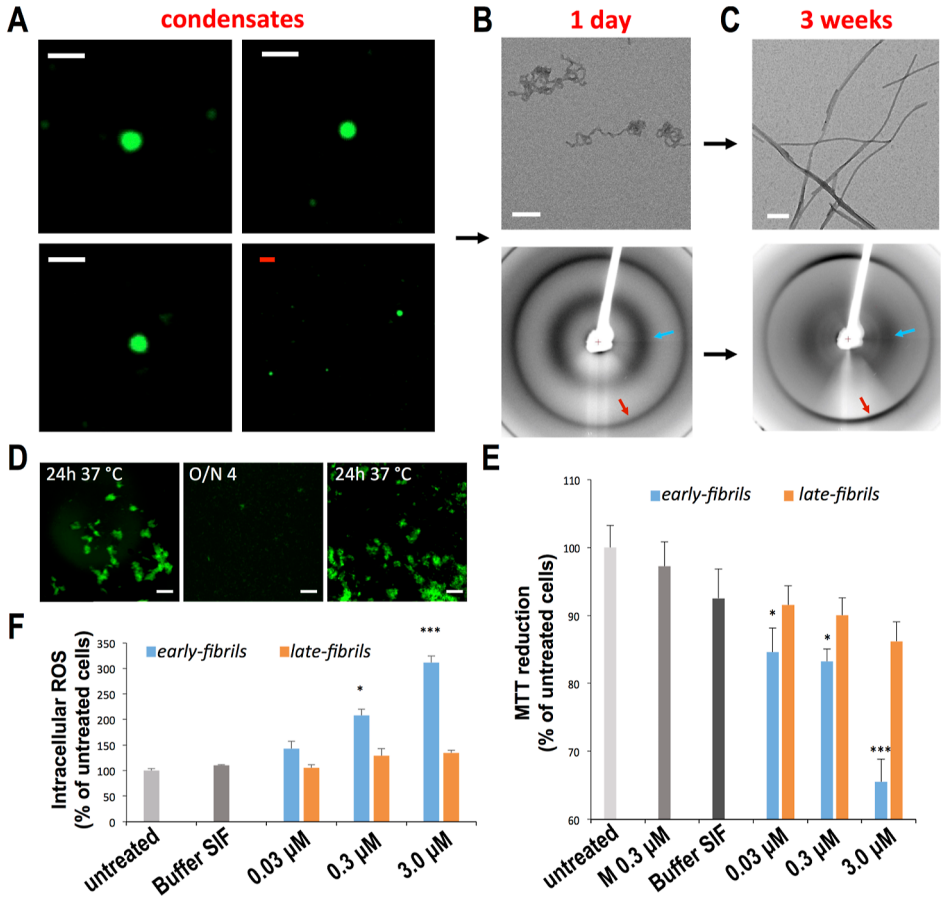

Figure 1. Properties of *early-fibrils* and *late-fibrils* from αS condensates. (A) Confocal images of spherical condensates of αS that readily form at 37 °C (see Experimental Section). The droplets show a round shape (see also Figure S1) and liquid-like properties in FRAP analyses (Figure S2). Samples included 1% of AF488-αS_{N122C} to fluorescently label the condensates. Scale bars are 1 μm (white) and 5 μm (red). (B) After 1 day of incubation, TEM images (top, scale bar 1 μm) showed the presence of curly *early-fibrils* that possess the typical X-ray diffraction pattern of amyloid fibrils (down), with reflections at 4.8 Å (red arrow) and 10 Å (cyan arrow). The diffraction patterns of the *early-fibrils* are typical of unoriented fibrillar samples, likely owing to the curly nature of these amyloids.[67] (C) After 3 weeks of incubation, TEM images (top, scale bar 1 μm) detected straight *late-fibrils*, with a conserved amyloid pattern of X-ray diffraction (down). (D) *early-fibrils* imaged at the confocal microscope (scale bar 20 μm) after 1 day of incubation at 37 °C. The aggregates disassemble after overnight incubation at 4 °C and can be observed again after 1 day of incubation at 37 °C. The sample included 2% of AF488-αS_{N122C} to fluorescently label the aggregates. (E) Cell dysfunction monitored by the reduction of MTT in human neuroblastoma SH-SY5Y cells upon incubation with increasing concentrations (0.03, 0.3, and 3 μM, monomer equivalents) of *early-fibrils* and *late-fibrils* from αS spherical condensates formed after 1 day and 3 weeks, respectively. * and *** indicate *P* values <0.05 and <0.001 with respect to untreated cells. Cells exposed to monomeric αS (M) and buffer of the *early-fibrils* (buffer SIF) were also shown. (F) Cell dysfunction monitored by intracellular ROS production in human neuroblastoma cells [details as in panel (E)]. Error bars in panels E and F are S.E.M.

synucleinopathies.[29−31] The biological properties of these fibrils, however, remain unclear, including their ability to induce neuronal toxicity. It is indeed becoming increasingly evident that mature αS fibrils may not be the crucial cytotoxic species in synucleinopathies, and that transient fibrils and oligomers formed during αS aggregation may be the source of the neurotoxicity observed in these neurodegenerative disorders.[2,32,33] Moreover, emerging evidence points to a role of condensation into αS liquid-like droplets as an initial step of aggregation[34−37] and evidence exists about a pathway of maturation from the condensate state into Lewy Bodies,[38] but the pathological relevance of these condensates has not yet been delineated. Understanding the evolution of αS condensates into mature fibrils and the biological properties of the aggregates forming during this process is therefore critical to identify the underlying molecular origins of synucleinopathies.

By combining solid-state NMR (ssNMR) spectroscopy, cryogenic electron microscopy (cryo-EM) and biophysical methods, along with other molecular and cellular biophysical techniques, we here characterized in vitro a structural-molecular pathway by which αS self-assembles into liquid-like droplets from which intermediate fibrils are rapidly formed. Upon extended incubation, mature αS amyloids appear in the mixture, showing the structural-topological properties of species analyzed post-mortem from patients' brains. The two types of αS fibrils generated during this aggregation process in vitro, designated as *early-fibrils* (intermediate) and *late-fibrils* (mature), possess significantly different conformational properties and induce different levels of cytotoxicity when incubated with SH-SY5Y cell lines. The structural characterization of these two fibrillar species enabled us to identify the critical molecular elements that endow the transient protofilaments, rather than the mature aggregates, with the ability to induce cellular toxicity. The evolution into mature *late-fibrils* was shown to significantly reduce the conformational dynamics as well as the interaction propensity

https://doi.org/10.1021/jacs.3c14703
J. Am. Chem. Soc. 2024, 146, 10537−10549

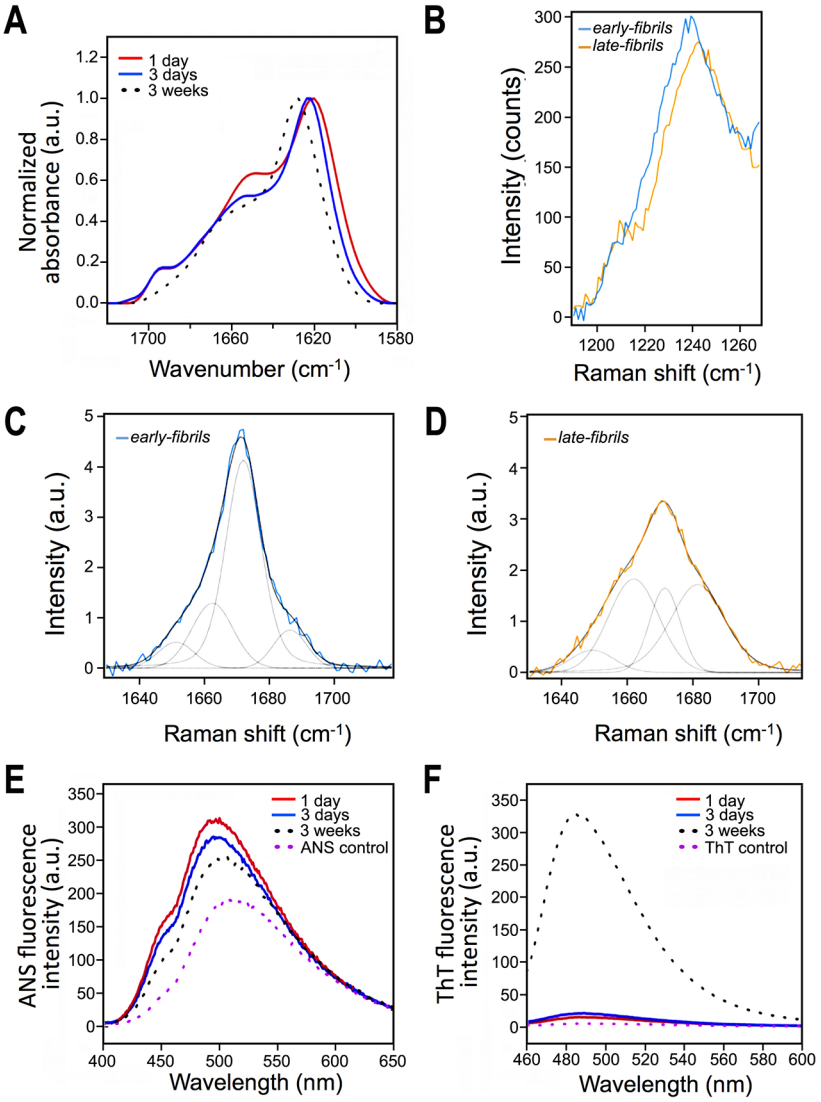

Figure 2. Secondary structure, hydrophobicity, and ThT binding of the *early-fibrils* and *late-fibrils* from αS condensates. (A) FT-IR spectra of αS upon incubation at the present experimental conditions at 37 °C. *Early-fibrils* after 1 and 3 days of incubation are shown in red and blue, respectively, whereas *late-fibrils* are shown in black-dotted line. The spectrum of the *early-fibrils* showed a band for antiparallel β-sheet structure at ca. 1685−1700 cm^{-1}, which is missing in the *late-fibrils*. (B) Raman spectra of the amide III band of *early-fibrils* (1 day of incubation, blue) and *late-fibrils* (3 weeks of incubation, orange). (C,D) Raman spectra of the amide I band region of the *early-fibrils* (C) and *late-fibrils* (D). Exemplary curve fitting (multipeakfit) of Raman spectra over the amide I region. Four fitting Lorentzian curves were employed for the convolution and assigned to α-helix (1650 cm^{-1}), parallel β-sheet (1662 cm^{-1}), antiparallel β-sheet (1672 cm^{-1}), and random coil (1685 cm^{-1}) structures.[39−41] In the case of the *early-fibrils*, the spectrum is dominated by the Lorentzian component at 1672 cm^{-1} (antiparallel β-sheet). In the case of the *late-fibrils* we observed a significant component in the Raman bands at 1662 cm^{-1} (parallel β-sheet) and 1685 cm^{-1} (random coil). The increased random coil component is attributed to the transfer of the *late-fibrils* from the incubation buffer into PBS to perform Raman measurements, which promoted the disassembly of the residual *early-fibrils*, thereby resulting in an increase of disordered monomers in the sample. (E) ANS binding assay spectra of *early-fibrils* and *late-fibrils* show a progressive reduction in fluorescence, which indicates a shielding of the hydrophobic regions, during the maturation of the aggregates. (F) ThT fluorescence reveals that both fibrils possess an amyloid core; however, the significantly stronger fluorescence of the *late-fibrils* indicates a larger core for these species compared to the *early-fibrils*.

of key protein regions such as the N-terminus of αS, making it no longer available to bind and promote the disruption of cellular membranes, a key step leading to downstream events such as the generation of reactive oxygen species, mitochondrial dysfunction, and calcium dyshomeostasis.

RESULTS

Evolution from αS Condensates into Mature Fibrils. In this study, we induced the self-assembly of αS in vitro at 37 °C using experimental conditions that promote rapid formation of spherical condensates of micrometer size and show liquid-like characteristics (Figures 1A and S1 and FRAP experiments Figure S2). After 1 day of incubation, curly fibrillar structures (*early-fibrils*) were distinctively observed in TEM images (Figure 1B). The *early-fibrils* showed an X-ray diffraction pattern characteristic of unoriented amyloid fibrils (Figure 1B), including 4.8 and 10 Å reflections, indicating that their core is stabilized by pairs of facing β-sheets. These fibrils were found to be vulnerable to external factors such as cold temperatures (Figure 1D), sonication, or transfer into PBS (Figure S3). By extension of the incubation for 3 weeks, straight amyloid aggregates (*late-fibrils*) with the typical cross-

https://doi.org/10.1021/jacs.3c14703
J. Am. Chem. Soc. 2024, 146, 10537−10549

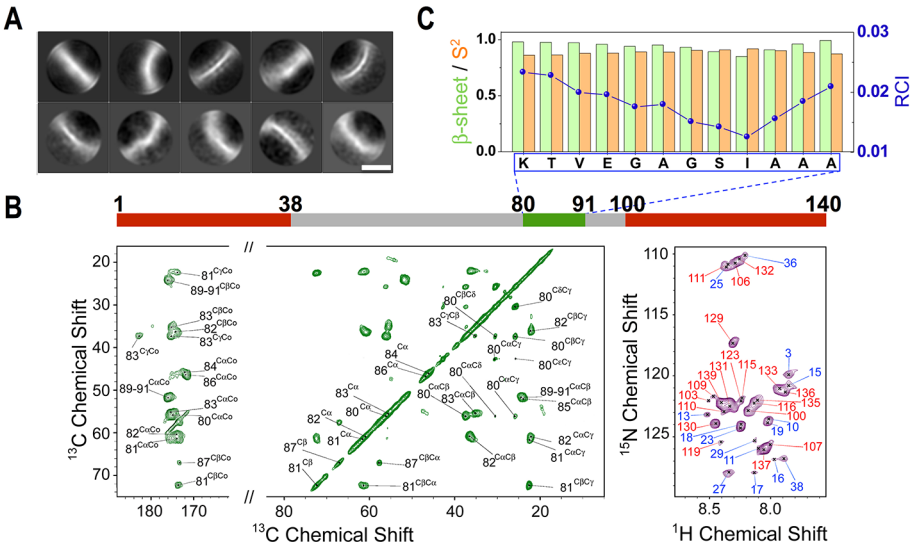

Figure 3. Structural topology of toxic *early-fibrils* from αS condensates. (A) Cryo-EM 2D class averages of the *early-fibrils* show heterogeneous particles with a variety of different curvatures. Scale bar 5 nm. (B) MAS ssNMR spectra of the *early-fibrils*. (left) $^{13}C-^{13}C$ DARR correlation spectra (aliphatic and carbonyl regions) measured using a 20 ms mixing time probed rigid regions in the core of the fibrils. (right) MAS $^{1}H-^{15}N$-HSQC spectra probed dynamical regions of the fibrils. MAS spectra were recorded at 5 °C at a MAS rate of 12.5 kHz. The bar on the top reports the protein regions detected in the spectra (green and red for the rigid and flexible regions, respectively). (C) Analysis of the ssNMR chemical shifts provided the β-sheet content (green),[57] order parameters S^2 (orange), and random coil index (blue)[58] of the core residues of the *early-fibrils*. The data indicate that the core is rigid and in a β-sheet conformation.

β X-ray diffraction pattern and an elongated morphology were observed in the sample (Figure 1C). In addition to distinct morphologies, the two types of fibrils showed different cytotoxicity properties. In particular, the *early-fibrils* of αS were found to impair the mitochondrial function (as observed with the MTT test, Figure 1E) and induce a significant amount of intracellular reactive oxygen species (ROS, Figure 1F) in a dose-dependent manner when incubated with SH-SY5Y neuroblastoma. By contrast, the *late-fibrils* showed very mild cytotoxic effects when incubated with SH-SY5Y cells.

To further investigate the structural properties of the two types of fibrils, we measured Fourier transform infrared (FT-IR) spectra and found that the core regions of *early-fibrils* and *late-fibrils* are topologically different (Figure 2A). In particular, the presence of an FT-IR peak at 1685 cm^{-1} suggested that the core of the *early-fibrils* is structured in an antiparallel β-sheet conformation, whereas the absence of this peak in the *late-fibrils* indicated a parallel β-sheet arrangement (Figure 2A). We also acquired Raman spectra (Figure 2B–D), which revealed significant differences in the amide I (Figure 2C,D) and amide III band regions (Figure 2B) of the two fibrillar forms of αS. In particular, the amide III Raman band in the *early-fibrils* presents a maximum centered at 1237 cm^{-1}, which is assigned to the antiparallel β-sheet structure, whereas in the *late-fibrils* the maximum of this band is shifted to 1242 cm^{-1}, accounting for a significant depletion of this antiparallel β-sheet structure (Figure 2B). In addition, by analyzing the amide I Raman band by the convolution of four fitting Lorentzian curves assigned to α-helix (1650 cm^{-1}), parallel β-sheet (1662 cm^{-1}), antiparallel β-sheet (1672 cm^{-1}), random coil (1685 cm^{-1}) structures,[39−41] we observed in the *early-fibrils* a dominancy of the band at 1672 cm^{-1} (antiparallel β-sheet) with a weak 1662 cm^{-1} band (parallel β-sheet, Figure 2C). By contrast, *late-fibrils* (Figure 2D) showed a significant component in the Raman bands at 1662 cm^{-1} (parallel β-sheet) and 1685 cm^{-1} (random coil), while the band at 1672 cm^{-1} appeared markedly reduced as compared to *early-fibrils*. Overall, FT-IR and Raman data consistently indicated the antiparallel nature of the αS *early-fibrils* in contrast to the parallel topology of the *late-fibrils*. Additional evidence for an antiparallel topology of the β-sheet of the *early-fibrils* was found using magic angle spinning (MAS) experiments in ssNMR (detailed below). In addition to the different morphologies and β-sheet topologies, the two fibrillar species presented other distinctive characteristics, including lower ANS binding (Figure 2E) and stronger ThT fluorescence (Figure 2F) in the *late-fibrils* compared to those of the early species. These results indicate that the mature species have minor exposure of hydrophobic regions and a more ordered and straighter fibrillar core than the early aggregates.

Taken together, these data delineate the properties of an aggregation process in which cytotoxic *early-fibrils* form transiently after αS condensation to subsequently evolve into mature *late-fibrils* presenting markedly different biophysical properties, such as morphology, structural core, exposure of hydrophobic regions, and cytotoxicity.

Detailed Structural Properties of Early and Late Fibrils from αS Condensates. In order to characterize at high resolution the structural properties of the *early-fibrils* forming in vitro from αS condensates, we employed cryo-EM, a technique that has recently solved a number of structures of αS amyloids.[25−31] Due to the heterogeneity in the local curvature of the curly *early-fibrils* of αS, however, atomic-resolution 3D maps could not be obtained for these aggregates, as 2D class averages demonstrate the poor alignment of these highly variable structures (Figures 3A and S4). We therefore used MAS ssNMR, a technique that has been successfully employed to elucidate the structure of amyloids[21] as well as oligomers[1] of αS. ssNMR resonances of carbon atoms of residues located in rigid regions of the *early-fibrils* were probed by using cross-polarization experiments. The $^{13}C-^{13}C$ DARR acquired with a mixing time of 20 ms showed well-resolved

https://doi.org/10.1021/jacs.3c14703
J. Am. Chem. Soc. 2024, 146, 10537−10549

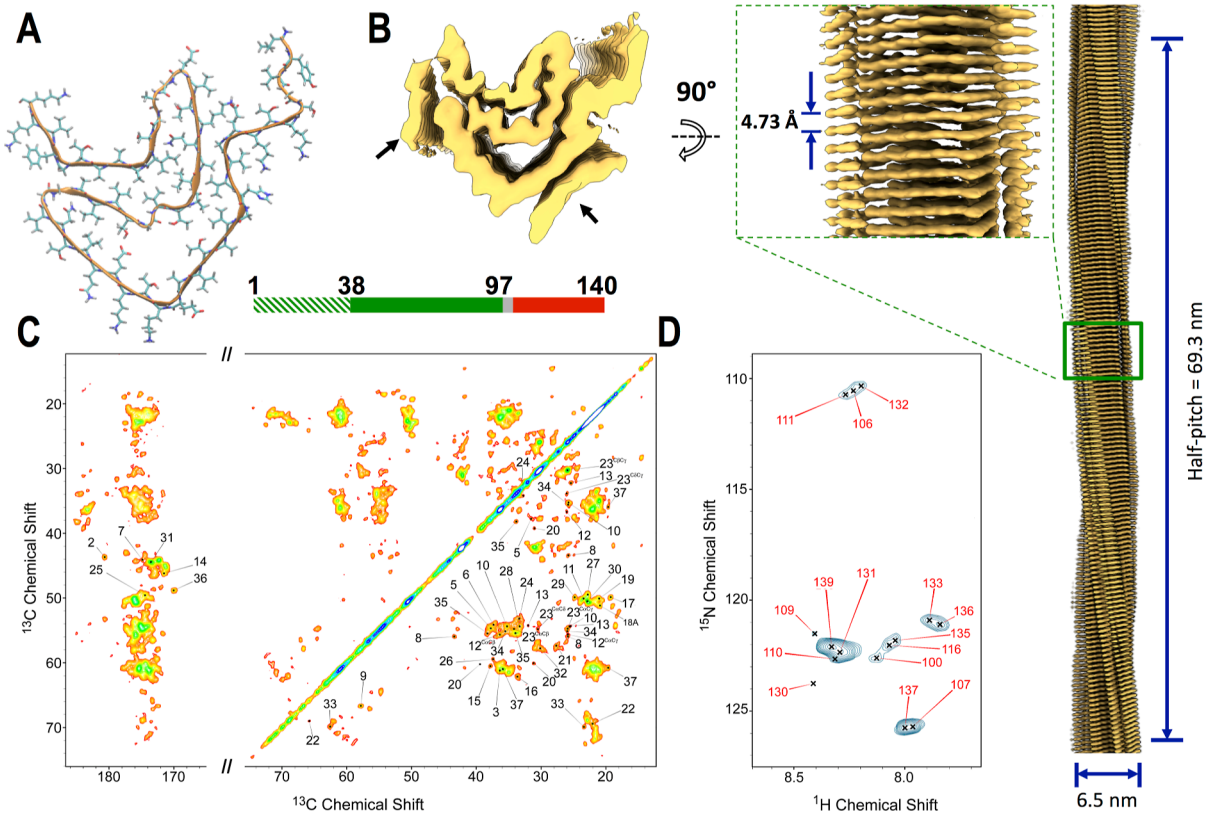

Figure 4. Structure of non-toxic *late-fibrils* from αS condensates. (A) Cryo-EM structure of *late-fibrils* resolved at 3.3 Å (PDB code: 8RI9). The structure, which is composed of one protein molecule in each stack of the fibril, is shown in the direction of the fibril axis. The atomic model, which spans residues 38 to 97, has a similar amyloid topology of αS fibrils studied postmortem from JOS patients[29] (Figure S11). (B) 3D density from the cryo-EM analysis shown from the top (left) and side (right) views (EMD code: 19184). Lower resolution density, indicated with black arrows, was not amenable for model building (Figure S10). The map was resolved with a half pitch of 69.3 nm. The average diameter of the fibrils is 6.3 nm. (C) MAS ssNMR ^{13}C−^{13}C DARR spectra (aliphatic and carbonyl regions) measured using a 20 ms mixing time probed rigid regions in the core of the *late-fibrils*. The spectra included peaks from the N-terminal region (labeled in the spectra), indicating that these are rigid and structured in the *late-fibrils*. In order to improve the peak shape, these spectra were measured using αS fibrils obtained by incubating fresh monomers with seeds generated from the *late-fibrils* by sonication. Unseeded spectra are shown in Figure S15. (D) MAS ssNMR ^{1}H−^{15}N-HSQC spectra probed the dynamical regions of the *late-fibrils*. MAS ssNMR spectra were recorded at 5 °C at a MAS rate of 12.5 kHz.

resonances for the *early-fibrils* of αS (Figures 3B and S5). Additional MAS ssNMR spectra based on the ^{15}N−^{13}C transfer, such as NCOCX or NCACX, presented enough signal-to-noise to prompt the resonance assignment, which revealed that the core of the *early-fibrils* is composed of the region 80-KTVEGAGSIAAA-91 (Figure S6 and Table S1). The analysis of the chemical shifts indicated that residues in the core of the *early-fibrils* adopt a rigid β-sheet conformation (Figure 3C), which is in agreement with the FT-IR and Raman spectra. By measuring ^{13}C−^{13}C DARR with a long mixing time (300 ms), we observed some cross-peaks that are not compatible with local sequential contacts in the αS chain (Figure S5). By measuring a 300 ms ^{13}C−^{13}C DARR on a sample prepared using 50% ^{13}C-labeled and 50% ^{12}C-unlabeled αS monomers, we could attribute these cross-peaks to intermolecular contacts in the *early-fibrils* (Figure S7A). These contacts between residues located on different β-strands prompted us to generate a molecular model that is fully consistent with an antiparallel β-sheet featuring an asymmetric distribution of the side chains, with a hydrophobic surface opposite to a hydrophilic side (Figure S7B). This model was further developed into a higher order assembly, based on the 10 Å reflection measured in the X-ray fiber diffraction pattern (Figure S8). The model includes two β-sheets stacked in a class 5 steric zipper[42] that is stabilized by a hydrophobic core and presents the hydrophilic side chains toward the solvent.

The *early-fibrils* were also found to possess a significant amount of highly mobile regions, as probed by ^{1}H−^{15}N-HSQC in combination with MAS ssNMR (Figure 3B). In particular, these spectra detected resonances from the N-terminus (regions 1−38) and the C-terminus (regions 100−140) of the αS sequence. The overlap between the ^{1}H−^{15}N-HSQC peaks in ssNMR measurements of the *early-fibrils* and those obtained in solution NMR for monomeric αS indicates that these regions maintain a disordered character in the fibrils. Taken together, our data delineate the topological properties of the *early-fibrils*, including an amyloid core in an antiparallel steric zipper flanked by disordered regions at the N- and C-termini.

We then applied cryo-EM and ssNMR to study the structural properties of the *late-fibrils*. The considerable morphological homogeneity of these aggregates favored the generation of high-quality 2D class averages (Figure S9), enabling a full-atomistic model to be refined from the 3D density maps (Figures 4A,B and S10). The analysis revealed the structure of a single protofilament for which we could build a 3D model spanning the region 38 to 97 of αS (Figure 4A). Additional density with low local resolution was observed

https://doi.org/10.1021/jacs.3c14703
J. Am. Chem. Soc. 2024, 146, 10537−10549

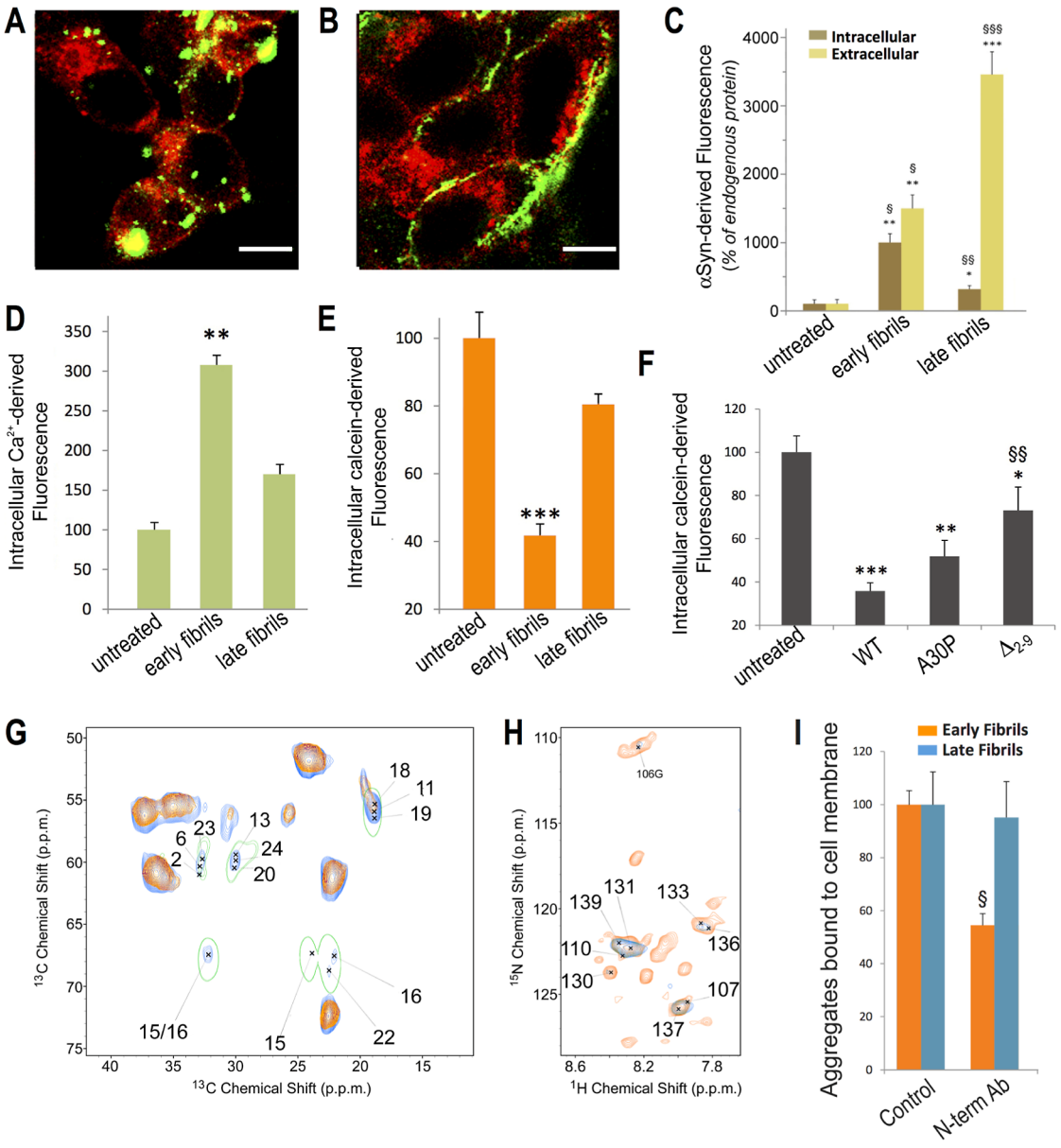

Figure 5. Mechanism of membrane interaction and cellular internalization. (A,B) Confocal microscopy images of the median plane of neuroblastoma cells incubated with *early-fibrils* (A) and *late-fibrils* (B) of αS (2% of AF488-αS_{N122C}) at 3 μM (monomer equivalents) for 1 h. Scale bar, 10 μm. (C) Internalization of *early-fibrils* and *late-fibrils* of αS (2% of AF488-αS_{N122C}) after 1 h of incubation at 3.0 μM (monomer equivalents) with neuroblastoma cells and estimated from confocal microscopy images of the median plane. *, **, and *** indicate $p < 0.5$, <0.01, and <0.001 versus untreated cells. (D) Intracellular Ca^{2+} levels (% of untreated cells) in control samples and in cells incubated with *early-fibrils* and *late-fibrils* of αS (3 μM of monomer equivalents) for 15 min ** indicates $P < 0.01$ versus untreated cells. (E) Membrane disruption monitored with the green fluorescent signal arising from the calcein probe loaded in neuroblastoma cells. The bars report the fluorescence values (% of untreated cells) of control samples and cells incubated with *early-fibrils* and *late-fibrils* of αS (3 μM of monomer equivalents) for 1 h. *** indicates $P < 0.001$ versus untreated cells. (F) Membrane disruption monitored with the calcein probe (% of untreated cells) in neuroblastoma cells incubated with *early-fibrils* of αS variants (WT, A30P, and Δ_{2-9}, 3 μM of monomer equivalents) for 1 h. These mutations did not affect the pathway of aggregation into *early-fibrils* and *late-fibrils* (Figure S16). ** and *** indicate $p < 0.01$ and 0.001 versus untreated cells. §§ indicates $p < 0.01$ versus cells treated with WT *early-fibrils*. (G) MAS ssNMR $^{13}C-^{13}C$-DARR spectra (spinning rate of 12.5 kHz; mixing time of 20 ms; contact time of 1 ms) of isolated *early-fibrils* of αS (orange) are overlapped with spectra of the membrane bound *early-fibrils* (blue). The latter were measured at −19 °C to enhance the signals of membrane-bound regions of the protein.[14,44,45] The $^{13}C-^{13}C$-DARR spectrum of the monomeric membrane-bound αS measured under the same conditions[44] is shown with a single green contour line. (H) MAS ssNMR $^{1}H-^{15}N$-HSQC spectrum of the *early-fibrils* of αS bound to lipid membranes (blue) detects only the C-terminal region of the protein. This is overlapped with the spectrum of isolated *early-fibrils* (orange). (I) Degree of membrane binding of *early-fibrils* (orange) and *late-fibrils* (blue) of αS measured following their incubation with human SH-SY5Y neuroblastoma cells for 1 h at 3.0 μM (monomer equivalents) in the absence or presence of 1:1 mol equiv of the N-terminal antibody. § indicates $p < 0.05$ versus cells treated with WT *early-fibrils*. Error bars in panels C, D, E, F, and I are S.E.M.

laterally on the protofilaments, suggesting that further regions in the αS sequence are structured around the core of the fibrils. The molecular model of the *late-fibrils* possessed a parallel β-sheet topology, which is in agreement with FT-IR and Raman spectra, and showed the characteristics of a type 1 αS amyloid polymorph.[43] The topological properties of the *late-fibrils* were

https://doi.org/10.1021/jacs.3c14703
J. Am. Chem. Soc. 2024, 146, 10537−10549

found to be consistent with those of single filaments studied postmortem from juvenile-onset synucleinopathy (JOS) patients (Figure S11).[29] The most similar region between the two structures spans residues 41 to 66 (rmsd of 1.12 Å, Cα atoms only, Figure S11C), including the first and second β-strands of the amyloid core. The orientation of lysine 58, a residue showing variable inward/outward pointing topologies across type 1 polymorphs,[43] was also found to match across the *late-fibrils* and JOS structures.

The overlap between these structures elucidates the nature of one of the two regions whose resolution in the *late-fibrils* map was too low to prompt model building (Figure S11A). Indeed, this region was resolved in the JOS structure as a fragment ranging from residues 14 to 21. In analogy, we postulate that the low-resolution density in the *late-fibrils* map is from N-terminal residues of the protein. Further evidence of the involvement of the N-terminal region in the core of the *late-fibrils* was provided by MAS ssNMR, where a large number of sharp peaks in the $^{13}C-^{13}C$ DARR spectra were detected (Figure 4C). In addition to region 38−97, the ssNMR spectra revealed the resonances of a segment of αS spanning residues 3 to 37, indicating that this region is rigid and highly structured in the *late-fibrils*. The structuralization of the N-terminal region in the *late-fibrils*, as evidenced from the cryo-EM density maps and MAS ssNMR spectra, is consistent with the analysis of the disordered regions of the fibrils via $^{1}H-^{15}N$-HSQC acquired using MAS ssNMR. In particular, these spectra identified exclusively peaks of the C-terminal region of the mature amyloids (Figure 4D), in contrast to the case of the *early-fibrils*, where also resonances from the N-terminal region were observed (Figure 3B). This evidence indicates that the N-terminus of the *late-fibrils* is not disordered and highly dynamical as in the case of the *early-fibrils*.

In addition to the JOS structure, *late-fibrils* were found to be topologically similar to type 1 monofilaments (polymorph 1 M) generated in vitro at pH 7.0 (Figure S12).[43] The observation of a monofilament topology, adopted by the *late-fibrils* at pH 7.4, suggests that the condensation of αS into liquid-like droplets may be associated with a local lowering of the pH, particularly because αS is an acidic protein that may create a more acidic pH value within an αS condensate.

Mechanism of Membrane Binding and Permeation by αS Early Fibrils. One of the main differences between *early-fibrils* and *late-fibrils* from αS condensates is that only the early species are able to cross the cellular plasma membrane (Figure 5A−C). In particular, upon incubation with neuroblastoma cells, 40% of the *early-fibrils* were found to penetrate the intracellular milieu, in contrast with only 7% observed for the *late-fibrils* (Figure 5C). The incubation of *early-fibrils* with SH-SY5Y cells is also associated with considerable disruption of the plasma membrane, as shown by an increase of 300% in the intracellular calcium levels, compared to 170% when using *late-fibrils* (Figure 5D), and a decrease of 60% of fluorescence in calcein-loaded cells, compared to 20% when using the *late-fibrils* (Figure 5E).

In order to characterize the structural basis of the membrane interaction of the *early-fibrils*, we employed MAS ssNMR to probe the rigid and dynamical regions of the fibrils upon binding with synaptic-like vesicles made of a mixture of DOPE/DOPS/DOPC lipids in a 5:3:2 molar ratio. The interaction with these vesicles has been extensively characterized for both the monomeric[14,44,45] and oligomeric[1] forms of αS, thus providing an opportunity for a direct comparison with the *early-fibrils*. $^{13}C-^{13}C$-DARR spectra of the vesicle-bound *early-fibrils* (Figure 5G) showed a number of additional peaks with respect to those of the isolated aggregates, thereby revealing the protein regions that are strongly bound to the membrane. These additional resonances were found to closely match with those of the N-terminal region of the membrane-bound αS adopting an amphipathic α-helical conformation.[44] In addition, ssNMR peaks of the N-terminus of αS were no longer observed in MAS $^{1}H-^{15}N$-HSQC when the *early-fibrils* were incubated with vesicles (Figure 5H), suggesting a local disorder-to-order transition upon membrane binding. Taken together, the ssNMR spectra suggest that the *early-fibrils* formed from αS condensates use the unstructured N-terminal region of the protein to bind tightly to the lipid membranes. This mechanism of membrane anchoring, an element also found in αS monomers[44] and toxic Type B* oligomers,[1] cannot be exploited by the *late-fibrils*, as the N-terminal region of these aggregates is structured around the fibril core (Figure 4). As *late-fibrils* are still able to bind the outer cellular membrane (Figure 5A−C), it is likely that their binding exploits different properties of the fibrils, e.g., the charge distribution on the fibril structure, leading to a different mechanism that preserves the membrane integrity.

Collectively, these data indicate that the maturation of the toxic *early-fibrils* into nontoxic late species deprives αS aggregates of a key element, the N-terminal region, to favor membrane anchoring and disruption. To verify this model, we used an antibody recognizing the N-terminal region of αS that was known to prevent its local membrane interaction.[46] In the presence of the antibody, we observed a 50% reduction of binding of the plasma membrane by the *early-fibrils*, while no effects were observed for the *late-fibrils*, corroborating the different role of the N-terminus in membrane binding by the two types of fibrils (Figure 5I). In agreement with our model, the antibody binding to the N-terminal region was found to reduce cellular toxicity and membrane disruption by the *early-fibrils* of αS (Figure S13). Further evidence in this context was obtained by producing aggregates composed of αS mutants that partially (αS_{A30P})[14] or severely ($\alpha S_{\Delta 2-9}$)[1] impair the local membrane affinity of the N-terminal region. The incubation of neuroblastoma cells with *early-fibrils* of αS_{WT}, αS_{A30P}, and $\alpha S_{\Delta 2-9}$ showed progressively milder membrane disruption effects (Figure 5F). These results therefore indicate that membrane anchoring via the exposed N-terminal region of αS in the *early-fibrils* is a critical step to induce cytotoxicity.

DISCUSSION

The characterization of the relevant species formed during αS aggregation is of critical importance to elucidate the biochemical mechanisms at the onset and development of synucleinopathies. A number of structural studies have elucidated the conformational properties of relevant aggregates of αS, such as toxic oligomers[1] or postmortem fibrils,[29−31] thus revealing the structural basis of its aggregation, but there is still poor understanding of the biological properties of these aggregates and their role in the neurotoxicity associated to the impairment of dopaminergic neurons in PD. Moreover, the properties of intermediate fibrils forming during αS self-assembly are still obscure due to the difficulties in their isolation, particularly when analyzing ex vivo aggregates from the brains of patients. Given the diversity and heterogeneity of the species forming during αS aggregation, or released by

https://doi.org/10.1021/jacs.3c14703
J. Am. Chem. Soc. 2024, 146, 10537−10549

fragmentation of mature amyloids,[33] it is likely that various forms of transient aggregates of αS have a role in mediating toxicity in neurons.[2] It is therefore critical to advance our understanding of the structural and interaction properties of elusive intermediate fibrillar species to elucidate their association with the neurotoxicity observed in the context of PD.

In this study, we elucidated the structural properties of intermediate fibrils of αS forming from liquid-like spherical condensates and evolving into mature amyloids having similar topological properties to fibrils analyzed post mortem from JOS patients.[29] The *early-fibrils*, unlike the late species, are reversible, as they form at 37 °C and dissolve at 4 °C. This propensity to cold denaturation[47,48] reflects the properties of the phase transitions of the spherical αS condensates that precede the insurgence of the *early-fibrils*, the latter forming very rapidly through the stabilization of a short antiparallel β-sheet core in the NAC region (80-KTVEGAGSIAAA-91). This region shares part of its sequence with the low-complexity AVEGAG motif that was identified for its propensity to promote β-sheet-stabilized phase transitions.[49] The presence of two glycine residues in the core of the transient aggregates may confer structural plasticity to these amyloids and allow for a variety of curvatures observed in these curly αS assemblies. By contrast, the core of the *late-fibrils* was found to adopt a completely different topology, which is composed of a series of stacked parallel β-sheets stabilizing straight amyloids that lack the temperature reversibility observed in the *early-fibrils*. The structural-topological differences between the two types of fibrils studied in this work also explain why the late species bind to the amyloid diagnostic dye ThT with a higher affinity than the *early-fibrils* and possess a lower hydrophobic exposure, as revealed from ANS binding (Figure 2).

By combining ssNMR spectroscopy and cryo-EM, along with other molecular and cellular biophysical techniques, we individuated the key structural elements that endow intermediate *early-fibrils* of αS with the ability to induce cytotoxicity and delineated the topological properties of the *late-fibrils* that prevent them from damaging the cellular membranes. In particular, we found that the exposure of the N-terminal region in a disordered and interaction-prone conformational state, in conjunction with the significant exposure of hydrophobic residues, provides the *early-fibrils* with a potent lipid-binding motif to establish strong interactions with the cellular membranes and consequently to disrupt their integrity. The large number of N-terminal tails exposed on the surface of the *early-fibrils* may enhance the membrane-binding affinity as a result of avidity effects, as observed in other contexts such as amyloid−nucleotide interactions.[50] We obtained evidence for the role of the exposed N-terminus of αS in the *early-fibrils* by showing that antibodies binding this region, as well as mutations that reduce its local membrane affinity, suppress the ability of these early aggregates to bind and disrupt the cellular membrane. As a result, through a mechanism of membrane binding and destabilization, the *early-fibrils* generate cytotoxicity by making the lipid-bilayer more permeable to Ca^{2+} ions and molecules as large as calcein, leading eventually to ROS production and mitochondrial impairment. By contrast, in the *late-fibrils* the N-terminal region was found to be structured around the amyloid core, which makes it unavailable to interact with membranes, thereby resulting in a different membrane-binding mechanism that does not perturb the integrity of the lipid bilayer. Consequently, cells exposed to *late-fibrils* are not permeable to Ca^{2+} ions and calcein as well as do not undergo ROS production and mitochondrial impairment.

CONCLUSIONS

In conclusion, the results of this study provide critical evidence that the cytotoxicity of αS aggregates is not a prerogative of oligomeric species but can also be induced by fibrils that possess specific structural properties, as found in the *early-fibrils*. These intermediate amyloid assemblies are indeed more similar to toxic αS oligomers[1] than to *late-fibrils* in terms of secondary structure, flexibility of the N-terminus, and exposure of hydrophobic residues. Upon maturation into the late species, the sequestration of the N-terminal region in the fibril core, and more generally the burial of the hydrophobic regions, reduce the ability of the aggregates to bind and disrupt lipid bilayers, thereby making the *late-fibrils* unable to disrupt membranes and induce cellular toxicity. Besides contributing toward the understanding of the origin of the pathological relevance of αS, these data also indicate that the crucial focus in amyloid research, including the design of therapeutic agents to suppress the toxicity of αS aggregates, should target the elusive intermediate species that are transiently formed during aggregation, as they induce the strongest neurotoxicity prior to evolving into mature amyoids that are less harmful to the cell.

EXPERIMENTAL SECTION

Production of αS Fibrils from Condensates. Recombinant αS with N-terminal acetylation was expressed in *E. coli* and purified as described previously.[44,51] Previous studies of αS condensation in vitro have employed crowding agents to induce protein self-assembly into liquid−liquid phase separations, including PEG at concentrations ranging from 10 to 20%.[34−36,38] Here, we exploited the salting-out effect to induce αS condensation in vitro. In particular, we incubated αS with 2-methyl-2,4-pentanediol (MPD), a compound largely used in protein crystallization[52] and phase separations,[53] as well as sulfate anions, which have been shown to enhance self-assembly of αS due to the kosmotropic effect.[54] More specifically, αS was first exchanged in water and then transferred into the incubation conditions, which include a protein concentration of 100 μM, 1× PBS buffer, pH 7.4, 0.02% (w/v) sodium azide, 0.5 M ammonium sulfate, and 10% (v/v) MPD. Under these buffer conditions, αS maintains the same solution NMR spectrum as observed in previous studies of the physiological binding to synaptic vesicles or plasma membrane[12,14,55] (Figure S14), which shows the typical peak distribution of intrinsically disordered proteins. The incubation was run at 37 °C for 1 to 3 days in the case of *early-fibrils* and at least 21 days for the *late-fibrils*. After the incubation, each sample was centrifuged (15 min, 16000 rpm), and the fibrillar pellet was washed twice before being resuspended in the appropriate volume of the respective buffer.

Magic Angle Spinning ssNMR. SsNMR data were measured using a 14.1T spectrometer equipped with a 3.2 mm E^{Free} probe (Bruker, Coventry, UK). Dipolar-assisted rotational resonance (DARR) spectra[56] were acquired at a magic angle spin (MAS) rate of 12.5 kHz with mixing times of 20, 50, 200, and 500 ms and with a 1 ms contact time. All of the spectra in this study were measured at 5 °C unless specified otherwise. Assignments of the ssNMR resonances of *early-fibrils* and *late-fibrils* of αS in the DARR spectra were obtained using a combination of 2D and 3D spectra (NCA, NCO, NCOCX, NCACX).

MAS ssNMR $^{1}H-^{15}N$-HSQC INEPT-based spectra were acquired using the same spectrometer settings as the CP-based spectra following previous setups.[51] Pulse widths were 2.5 μs for ^{1}H and 5.5 μs for ^{13}C, and ^{1}H TPPM decoupling was applied at $\omega_{rf}/(2\pi)$ = 71.4−100 kHz.[44] Assignments of the resonances of *early-fibrils* and *late-fibrils* αS in the $^{1}H-^{15}N$-HSQC spectra were obtained by overlap

https://doi.org/10.1021/jacs.3c14703
J. Am. Chem. Soc. 2024, 146, 10537−10549

with the monomer solution NMR $^{1}H-^{15}N$-HSQC as well as from previous ssNMR studies of monomeric αS bound to the membrane, i.e., showing the resonances of the C-terminal region in these spectra.[51]

To address the secondary-structure properties of the protein regions probed by ssNMR CP, we employed the δ2D method[57] to analyze the backbone chemical shifts of the core regions (Cα, Cβ, N, and CO). Chemical shifts were also employed to analyze the local dynamics and order parameters S^2 using the RCI method.[58]

Cryo-EM Sample Preparation, Data Collection, and Helical Reconstruction. 3 μL of αS *early-fibrils* or *late-fibrils* samples were applied to 300 mesh Cu Quantifoil R2/2 grids previously treated with glow discharge. The grids were frozen by plunging into liquid ethane using a Vitribot mark IV set to a 5 s blot time, blot force of 3, and a wait time of 60 s. Micrographs were collected by using a Titan Krios 300 kV microscope equipped with a Falcon III detector in counting mode. See Tables S2 and S3 for data collection parameters. Images were aligned using MotionCor2, and CTF was estimated with CTFFind4.[59,60] All subsequent steps of helical reconstruction were performed in RELION 3.0[61] unless otherwise specified. All fibrils were picked manually to ensure that helical reconstruction was performed on a single dominant polymorph. Several rounds of 2D classification were used to select the best particles for the 3D reconstruction. Successive rounds of 3D classification further removed noisy or ambiguous fibril segments. The final refined helical reconstruction was filtered with a *B*-factor of −200 using postprocessing. For complete details of the processing parameters used, refer to Table S2.

Cryo-EM Model Building. A model of the β-sheet polypeptide was fitted and refined within the available density. Model 6H6B from the Protein Data Bank (PDB) was used as an initial model within the reconstructed EM density.[62] A single polypeptide model was further refined using REFMAC5 and Coot within the CCP-EM suite.[63−65] This model was replicated across five β-sheets in the reconstructed density using MOLREP. The five polypeptides were then further refined using ISOLDE within UCSF Chimera X[66] to produce the final model. The structure of the *late-fibrils* has been deposited in the Protein Data Bank (PDB code: 8RI9). The cryo-EM density maps have been deposited in the Electron Microscopy Data Bank (accession code: 19184).

Negative-Stain EM. Five μL of samples of αS *early-fibrils* or *late-fibrils* were applied to freshly glow discharged carbon-supported 300 mesh copper grids (Agar Scientific Ltd., Essex, UK). The sample was incubated for 1 min prior to blotting excess liquid with filter paper before applying 5 μL of a 2% uranyl acetate stain solution for a further 1 min. Excess stain was blotted, and grids were left to dry for 5 min prior to imaging. Micrographs were collected on a Tecnai T12 TWIN microscope (Thermo Fisher Scientific) operating at 120 kV with a F216 TVIPS CCD camera.

X-ray Fiber Diffraction. The solution of αS *early-fibrils* or *late-fibrils* was vortexed, and a droplet of 10 μL was placed between two wax-tipped capillary tubes and left to dry overnight.[67] X-ray diffraction images were collected using a Rigaku MicroMax 007-HF high-flux generator on a Rigaku Saturn 944+ CCD detector.

Small Unilamellar Vesicles. Small unilamellar vesicles (SUVs) were prepared from chloroform solutions of 1,2-dioleoyl-*sn*-glycero-3-phosphoethanolamine (DOPE), 1,2-dioleoyl-*sn*-glycero-3-phospho-L-serine (DOPS), and 1,2-dioleoyl-*sn*-glycero-3-phosphocholine (DOPC, Avanti Polar Lipids Inc., Alabaster, AL, USA) mixed at molar ratios of 5:3:2. After evaporation of chloroform under a nitrogen stream, a thin lipid film was obtained by drying under a vacuum. A water solution of the lipids was then obtained by adding aqueous buffer (20 mM sodium phosphate, pH 6.0) to the dried thin film at a final lipid concentration of 15 mg·mL^{-1} (1.5%), followed by vortex mixing. To obtain vesicles of the size of ∼50 nm, the solution was subjected to freeze−thawing cycles and subsequently to sonication until the liquid became clear.[44,68]

Analytical Ultracentrifugation. Analytical ultracentrifugation (AUC) was performed using a Beckman−Coulter Optima XL-I analytical ultracentrifuge equipped with UV−visible absorbance optics and an An 50 Ti rotor. Experiments were carried out at 20 °C using rates of 38,000 to 43,000 rpm (106,750−136,680*g*) to measure the sedimentation velocities of the samples. Sedimentation velocity experiments were carried out after 6 h of incubation of the protein samples at concentrations ranging from 40 to 80 μM in their respective buffers. We used least-squares boundary modeling of sedimentation velocity data to calculate sedimentation coefficient distributions corrected for standard conditions. The model used the c(s) and ls-g*(s) methods in SEDFIT (https://sedfitsedphat.github.io/).

Fourier Transform Infrared Spectroscopy. αS *early-fibrils* and *late-fibrils* were characterized with FT-IR in PBS at pH 7.4 at a concentration of 400 μM (monomer equivalents), using a Bruker BioATRCell II and a Bruker Equinox 55 FT-IR spectrophotometer (Bruker Optics Limited, Coventry, UK) equipped with a liquid nitrogen-cooled mercury cadmium telluride (MCT) detector and a silicon internal reflection element (IRE). 256 interferograms were collected for each sample at a resolution of 2 cm^{-1}. The contribution of the buffer to the signal was independently measured and subtracted during data analysis. The curve fitting of the amide I region (1720−1580 cm^{-1}) was carried out with an Opus instrument (Bruker Optics Limited, Coventry, UK). The data in Figure 2A show FT-IR spectra of αS upon incubation under the present experimental conditions. After 1 day, the mixture is primarily dominated by *early-fibrils* (red), showing a peak at 1654 cm^{-1} that is indicative of disordered regions, a band for intermolecular β-sheet structure at ca. 1615−1620 cm^{-1} and a band for antiparallel β-sheet structure at ca. 1685−1700 cm^{-1}. After 3 days, the FT-IR spectrum is essentially unchanged (blue), except for the reduction in the intensity of the band associated with disordered regions. After 3 weeks, the mixture is primarily dominated by *late-fibrils* (black-dotted), showing a shift in the intermolecular β-sheet band at 1615−1620 cm^{-1} and the depletion of the antiparallel band at ca. 1615−1620 cm^{-1}, overall indicating a conversion into parallel fibrils and a further reduction of the band associated with disordered regions.

Fluorescence Recovery after Photobleaching. Fluorescence recovery after photobleaching (FRAP) measurements were acquired using a Zeiss microscope LSM 980 with an Airyscan 2 at a constant temperature of 37 °C. αS samples for these experiments were prepared using a 1:100 molar ratio of Alexa Fluor 488-labeled (AF488-αS_{N122C}) to unlabeled protein. Each FRAP experiment involved 3 prebleach frames followed by 5 bleach frames, and recovery was monitored over 10 min (one frame each 30 s).

Differential Interference Contrast and Confocal Microscopy. Five μL of the αS sample were spotted onto a microscope slide 5 min after starting the incubation at 37 °C. The slides were covered with a 12 mm glass coverslip and immediately visualized using a TCS SP8 scanning confocal microscopy system (Leica Microsystems) under DIC mode. In another set of experiments, monomeric αS, including 2% of AF488-αSN122C, was incubated for 24 h at 37 °C to form *early-fibrils*, which were further incubated overnight at 4 °C and finally put again at 37 °C for another 24 h. At each time point, 5 μL of the protein sample were spotted onto microscope slides as reported previously and then visualized with a TCS SP8 scanning confocal microscopy system (Leica Microsystems) equipped with an argon laser source. Fluorescence emission was detected after excitation at 488 nm. In another set of experiments, DIC and confocal microscopy images were simultaneously acquired on the same assemblies and merged by superimposition.

Fluorescence Measurements of ANS and ThT Binding. Fluorescence spectra for 8-anilino-1-naphthalenesulfonic (ANS) and thioflavin T (ThT) binding measurements were acquired using a Varian Cary Eclipse instrument (Palo Alto, CA, USA). The spectrofluorimeter includes a temperature-controlled cell holder utilizing a 2 mm × 10 mm path length cuvette. Fluorescence derived from ThT binding was measured using an excitation of 446 nm and an emission fluorescence from 460 to 600 nm. Ten μM of each protein sample was incubated with 50 μM ThT in PBS for 30 min before fluorescence recording. The data in Figure 2F show that while *early-fibrils* induce ThT fluorescence, indicating the presence of an

https://doi.org/10.1021/jacs.3c14703
J. Am. Chem. Soc. 2024, 146, 10537−10549

amyloid core, the fluorescence of the *late-fibrils* is significantly stronger, indicating a core involving considerably larger portions of the protein. These data are in agreement with the high-resolution ssNMR and cryo-EM analyses of this study. ANS binding was monitored by exciting the sample at 350 nm and recording the emission from 400 to 650 nm. In this case, a 5 μM protein sample was incubated with 250 μM ANS in PBS for 30 min before recording the spectra. The extinction coefficient at 350 nm of ANS was taken to be 5000 cm^{-1} M^{-1}. For the analysis of ANS binding to the different protein samples in the presence of urea, the samples were initially incubated for at least 2 h with urea before the addition of ANS. ANS fluorescence spectra (Figure 2E) show a progressive reduction in fluorescence, hence the exposed hydrophobic regions, in the aggregates. These data indicate that the conversion from *early-fibrils* to *late-fibrils* is therefore associated with shielding of the hydrophobic regions.

Cell Cultures. Authenticated human neuroblastoma SH-SY5Y cells were purchased from A.T.C.C. (Manassas, VA, USA; the company has performed the authentication of the cell line). We tested that cells were free from mycoplasma contamination prior to culturing them in Dulbecco's modified Eagle's medium (DMEM), F-12 HAM with 25 mM HEPES and $NaHCO_3$ (1:1), supplemented with 10% FBS, 1 mM glutamine, and 1.0% antibiotics.[46,69] SH-SY5Y cells were incubated at 37 °C in a 5% CO_2 humidified atmosphere. Cultures were grown until they reached 80% confluence for a maximum of 20 passages.[46,69]

MTT Reduction Assay. The cytotoxicity of the αS *early-fibrils* and *late-fibrils*, when incubated with SH-SY5Y cells, was assessed using the 3-(4,5-dimethylthiazol-2-yl)-2,5-diphenyltetrazolium bromide (MTT) assay in 96-well plates.[46,69] Briefly, increasing concentrations (0.03, 0.3, and 3 μM, monomer equivalents) of both types of αS fibrils were added to the cultured cells for 24 h. After the incubation, we removed the culture medium and washed the cells with PBS. Subsequently, cell viability by the MTT assay was expressed as the percentage of MTT reduction in treated cells with respect to untreated samples (taken as 100%), as previously reported.[46,69]

ROS Measurements. The generation of ROS induced by the αS *early-fibrils* and *late-fibrils* was monitored in SH-SY5Y cells seeded on glass coverslips following the incubation with increasing concentrations of aggregates (0.03, 0.3, and 3 μM, monomer equivalents) for 15 min. After treatment, SH-SY5Y cells were washed using PBS and loaded with 10 μM 2′,7′-dichlorodihydrofluorescein diacetate (CM-H_2DCFDA, Life Technologies, CA, USA) as previously described.[46] We then used the TCS SP8 scanning confocal microscopy system (Leica Microsystems) equipped with an argon laser source to detect fluorescence (using an excitation at 488 nm). Using a Leica Plan Apo 63× oil immersion objective, for each sample a series of 1.0 μm thick optical sections (1024 × 1024 pixels) was taken through the cell depth. These sections were projected to obtain a single composite image by superimposition. Acquisition conditions, such as pinhole diameters, detector gain, and laser powers, were optimized in the confocal microscope prior acquisition and kept constant throughout the analysis. ImageJ software (NIH, Bethesda, MD, USA) (Rasband 1997−2008) was employed to analyze the images. Intensities of fluorescence in each sample were expressed in percentages and normalized with the values measured in untreated cells (taken as 100%).

Imaging and Quantification of αS Fibrils Bound to the Plasma Membrane and Internalized into Cytosol. αS *early-fibrils* and *late-fibrils* at a concentration of 3 μM (monomer equivalents) were incubated for 15 min with SH-SY5Y cells seeded on glass coverslips. Cells were subsequently washed with PBS and counterstained for 15 min by using 5.0 $\mu g \cdot mL^{-1}$ Alexa Fluor 633-conjugated wheat germ agglutinin. This molecule is specific to fluorescently label the plasma membrane of the cells (Life Technologies, CA, USA).[46,70] Cells were then washed using PBS and fixed in 2% (w/v) buffered paraformaldehyde for 10 min at room temperature (20 °C). αS fibrils were detected by direct fluorescence using 2% AF488-αS_{N122C} in the monomer mixture prior to the aggregation. To detect αS aggregates bound to the cell surface, the cellular membrane was not permeabilized at this stage, thus preventing antibody internalization. To detect both species bound to the cell membrane and internalized into the cytosol, the membrane was permeabilized with glycerol at 3.0% (v/v). Images were acquired after double-excitation at 488 and 633 nm, by using the scanning confocal microscopy described above, and the intracellular and extracellular green fluorescences were expressed as the percentage of fluorescence measured in untreated cells (taken as 100%).

Intracellular Ca^{2+}. The influx of Ca^{2+} ions from the extracellular space into the cytosol was monitored in SH-SY5Y cells seeded on glass coverslips, following the incubation with αS *early-fibrils* and *late-fibrils* (3 μM, monomer equivalents) for 15 min. After treatment, the cells were washed with PBS and loaded with 10 μM Fluo-4 AM (Thermo Fisher Scientific) as previously reported.[69] Cell fluorescence was detected after excitation at 488 nm by the confocal microscopy system described above and expressed as the percentage of fluorescence measured in untreated cells (taken as 100%).

Cellular Membrane Permeabilization by Calcein-Derived Fluorescence. The integrity of the cellular membrane in SH-SY5Y cells was monitored by an established method, where the calcein-AM probe passively crosses the cell membrane and is hydrolyzed by cellular esterases into calcein, a polar green-fluorescent molecule. Calcein is retained by cells having an intact membrane, whereas in the case of membrane disruption, it is released by the cell, corresponding to an observable loss of fluorescence. In this experiment, 2.0 μM calcein-AM (Molecular Probes) were diluted in the culture medium of SH-SY5Y cells seeded on glass coverslips for 20 min at 37 °C.[69,70] Subsequently, the cells were incubated for 1 h with αS *early-fibrils* and *late-fibrils* (3 μM, monomer equivalents). Using the TCS SP8 scanning confocal microscopy system (Leica Microsystems) described above, fluorescence emission was detected upon excitation at 488 nm with an argon laser source.

Raman Spectroscopy. αS samples (100 μM in PBS solution) were drop-casted to measure Raman spectra using a LabRam HR800Evo (Horiba) system coupled to a 633 nm wavelength laser with a 600-grooves/mm grating. A 100× microscope objective with 0.9 NA, generating a 1 μm laser beam waist and a laser power at the sample of 8.4 mW, was used to collect backscattered light. Each spectrum was acquired for 10 s and accumulated 10 times. αS solution was deposited through a 5 μL drop onto a silver mirror support (Thorlabs, Inc., Newton, NJ). Subsequently, the samples were allowed to dry in air for 20 min. Raman spectra were then acquired from the outer ring of the dried drop. A semiquantitative estimation of the secondary structure of the samples was obtained through a fitting procedure of the amide I spectral region, resulting from the convolution of bands centered at 1655 cm^{-1} for α-helices, 1660−1675 cm^{-1} for organized β-sheets, and 1685 cm^{-1} for random structure.[71]

■ ASSOCIATED CONTENT

Supporting Information

The Supporting Information is available free of charge at https://pubs.acs.org/doi/10.1021/jacs.3c14703.

Confocal microscopy (fluorescence and DIC); FRAP; AUC; Cryo-EM micrographs; MAPS and helical reconstruction; ssNMR DARR HNCACX, HNCOCX, and CHHC; molecular modeling; structural comparisons of αS amyloids; cellular toxicity (MTT and membrane disruption); and solution NMR HSQC spectrum (PDF)

■ AUTHOR INFORMATION

Corresponding Authors

Giuliana Fusco − *Department of Chemistry, University of Cambridge, Cambridge CB2 1EW, U.K.; Department of Pharmacy, University of Naples, Naples 80131, Italy;*

https://doi.org/10.1021/jacs.3c14703
J. Am. Chem. Soc. 2024, 146, 10537−10549

orcid.org/0000-0002-3644-9809; Email: gf203@cam.ac.uk

Alfonso De Simone − *Department of Life Sciences, Imperial College London, London SW7 2AZ, U.K.; Department of Pharmacy, University of Naples, Naples 80131, Italy;* orcid.org/0000-0001-8789-9546; Email: alfonso.desimone@unina.it

Authors

Serene W. Chen − *Department of Life Sciences, Imperial College London, London SW7 2AZ, U.K.;* Present Address: Bioprocessing Technology Institute, 20 Biopolis Way, #06-01 Centros, Singapore 138668

Joseph D. Barritt − *Department of Life Sciences, Imperial College London, London SW7 2AZ, U.K.;* orcid.org/0000-0002-4311-5305

Roberta Cascella − *Department of Experimental and Clinical Biomedical Sciences, Section of Biochemistry, University of Florence, Florence 50134, Italy;* orcid.org/0000-0001-9856-6843

Alessandra Bigi − *Department of Experimental and Clinical Biomedical Sciences, Section of Biochemistry, University of Florence, Florence 50134, Italy;* orcid.org/0000-0002-1067-6288

Cristina Cecchi − *Department of Experimental and Clinical Biomedical Sciences, Section of Biochemistry, University of Florence, Florence 50134, Italy;* orcid.org/0000-0001-8387-7737

Martina Banchelli − *Institute of Applied Physics "Nello Carrara" National Research Council of Italy, Florence 50019, Italy;* orcid.org/0000-0001-5348-0552

Angelo Gallo − *Department of Chemistry, University of Turin, Turin 10124, Italy;* orcid.org/0000-0001-9778-4822

James A. Jarvis − *Department of Life Sciences, Imperial College London, London SW7 2AZ, U.K.; Randall Centre for Cell and Molecular Biophysics and Centre for Biomolecular Spectroscopy, King's College London, London SE1 9RT, U.K.*

Fabrizio Chiti − *Department of Experimental and Clinical Biomedical Sciences, Section of Biochemistry, University of Florence, Florence 50134, Italy;* orcid.org/0000-0002-1330-1289

○**Christopher M. Dobson** − *Department of Chemistry, University of Cambridge, Cambridge CB2 1EW, U.K.*

Complete contact information is available at: https://pubs.acs.org/10.1021/jacs.3c14703

Author Contributions

♦S.W.C. and J.D.B. contributed equally to this work.

Notes

The authors declare no competing financial interest.

○Deceased on September the 8th, 2019.

■ ACKNOWLEDGMENTS

This research was supported by the European Research Council (ERC—BioDisOrder—819644 to A.D.S.), Italian Ministry of University and Research (MUR) (Rita Levi Montalcini Programme to G.F.), and University of Florence (Fondi di Ateneo to R.C., C.C. and F.C.). Work was also supported by #NEXTGENERATIONEU (NGEU) and funded by the Italian MUR, National Recovery and Resilience Plan (NRRP), project MNESYS (PE0000006)—A Multiscale integrated approach to the study of the nervous system in health and disease (D.R. 1553 11.10.2022; to R.C. and C.C.) and Investment PE8—Project Age-It: "Ageing Well in an Ageing Society" (D.R. 1557 11.10.2022; to A.B. and F.C.). We are grateful to Dr Sjors H. W. Scheres (Laboratory of Molecular Biology, UK) and Dr Luigi Vitagliano (National Research Council of Italy) for discussions.

■ REFERENCES

(1) Fusco, G.; Chen, S. W.; Williamson, P. T. F.; Cascella, R.; Perni, M.; Jarvis, J. A.; Cecchi, C.; Vendruscolo, M.; Chiti, F.; Cremades, N.; Ying, L.; Dobson, C. M.; De Simone, A. Structural basis of membrane disruption and cellular toxicity by α-synuclein oligomers. *Science* **2017**, *358* (6369), 1440−1443.

(2) Lashuel, H. A.; Overk, C. R.; Oueslati, A.; Masliah, E. The many faces of α-synuclein: from structure and toxicity to therapeutic target. *Nat. Rev. Neurosci.* **2013**, *14* (1), 38−48.

(3) Spillantini, M. G.; Schmidt, M. L.; Lee, V. M.; Trojanowski, J. Q.; Jakes, R.; Goedert, M. α-Synuclein in Lewy bodies. *Nature* **1997**, *388* (6645), 839−840.

(4) Newberry, R. W.; Leong, J. T.; Chow, E. D.; Kampmann, M.; DeGrado, W. F. Deep mutational scanning reveals the structural basis for α-synuclein activity. *Nat. Chem. Biol.* **2020**, *16* (6), 653−659.

(5) Luk, K. C.; Kehm, V.; Carroll, J.; Zhang, B.; O'Brien, P.; Trojanowski, J. Q.; Lee, V. M. Pathological α-Synuclein Transmission Initiates Parkinson-like Neurodegeneration in Nontransgenic Mice. *Science* **2012**, *338* (6109), 949−953.

(6) Chiti, F.; Dobson, C. M. Protein Misfolding, Amyloid Formation, and Human Disease: A Summary of Progress Over the Last Decade. *Annu. Rev. Biochem.* **2017**, *86*, 27−68.

(7) Uversky, V. N.; Eliezer, D. Biophysics of Parkinsons Disease: Structure and Aggregation of α- Synuclein. *Curr. Protein Pept. Sci.* **2009**, *10* (5), 483−499.

(8) Galvin, J. E.; Schuck, T. M.; Lee, V. M.; Trojanowski, J. Q. Differential Expression and Distribution of α-β-and γ-Synuclein in the Developing Human Substantia Nigra. *Exp. Neurol.* **2001**, *168* (2), 347−355.

(9) Burre, J.; Sharma, M.; Tsetsenis, T.; Buchman, V.; Etherton, M. R.; Sudhof, T. C. α-Synuclein Promotes SNARE-Complex Assembly in Vivo and in Vitro. *Science* **2010**, *329* (5999), 1663−1667.

(10) Auluck, P. K.; Caraveo, G.; Lindquist, S. α-Synuclein: Membrane Interactions and Toxicity in Parkinson's Disease. *Annu. Rev. Cell Dev. Biol.* **2010**, *26*, 211−233.

(11) Diao, J.; Burre, J.; Vivona, S.; Cipriano, D. J.; Sharma, M.; Kyoung, M.; Sudhof, T. C.; Brunger, A. T. Native α-synuclein induces clustering of synaptic-vesicle mimics via binding to phospholipids and synaptobrevin-2/VAMP2. *eLife* **2013**, *2*, No. e00592.

(12) Man, W. K.; Tahirbegi, B.; Vrettas, M. D.; Preet, S.; Ying, L.; Vendruscolo, M.; De Simone, A.; Fusco, G. The docking of synaptic vesicles on the presynaptic membrane induced by α-synuclein is modulated by lipid composition. *Nat. Commun.* **2021**, *12* (1), 927.

(13) Cooper, A. A.; Gitler, A. D.; Cashikar, A.; Haynes, C. M.; Hill, K. J.; Bhullar, B.; Liu, K.; Xu, K.; Strathearn, K. E.; Liu, F.; Cao, S.; Caldwell, K. A.; Caldwell, G. A.; Marsischky, G.; Kolodner, R. D.; Labaer, J.; Rochet, J. C.; Bonini, N. M.; Lindquist, S. α-Synuclein Blocks ER-Golgi Traffic and Rab1 Rescues Neuron Loss in Parkinson's Models. *Science* **2006**, *313* (5785), 324−328.

(14) Fusco, G.; Pape, T.; Stephens, A. D.; Mahou, P.; Costa, A. R.; Kaminski, C. F.; Kaminski Schierle, G. S.; Vendruscolo, M.; Veglia, G.; Dobson, C. M.; De Simone, A. Structural basis of synaptic vesicle assembly promoted by a-synuclein. *Nat. Commun.* **2016**, *7*, 12563.

(15) Maltsev, A. S.; Chen, J.; Levine, R. L.; Bax, A. Site-Specific Interaction between α-Synuclein and Membranes Probed by NMR-Observed Methionine Oxidation Rates. *J. Am. Chem. Soc.* **2013**, *135* (8), 2943−2946.

(16) Plotegher, N.; Gratton, E.; Bubacco, L. Number and Brightness analysis of alpha-synuclein oligomerization and the associated mitochondrial morphology alterations in live cells. *Biochim. Biophys. Acta* **2014**, *1840* (6), 2014−2024.

(17) Mahul-Mellier, A. L.; Burtscher, J.; Maharjan, N.; Weerens, L.; Croisier, M.; Kuttler, F.; Leleu, M.; Knott, G. W.; Lashuel, H. A. The process of Lewy body formation, rather than simply α-synuclein fibrillization, is one of the major drivers of neurodegeneration. *Proc. Natl. Acad. Sci. U.S.A.* **2020**, *117* (9), 4971−4982.
(18) Lee, S.-J.; Masliah, E. Neurodegeneration: Aggregates feel the strain. *Nature* **2015**, *522* (7556), 296−297.
(19) Chartier-Harlin, M. C.; Kachergus, J.; Roumier, C.; Mouroux, V.; Douay, X.; Lincoln, S.; Levecque, C.; Larvor, L.; Andrieux, J.; Hulihan, M.; Waucquier, N.; Defebvre, L.; Amouyel, P.; Farrer, M.; Destee, A. α-synuclein locus duplication as a cause of familial Parkinson's disease. *Lancet* **2004**, *364* (9440), 1167−1169.
(20) Singleton, A. B.; Farrer, M.; Johnson, J.; Singleton, A.; Hague, S.; Kachergus, J.; Hulihan, M.; Peuralinna, T.; Dutra, A.; Nussbaum, R.; Lincoln, S.; Crawley, A.; Hanson, M.; Maraganore, D.; Adler, C.; Cookson, M. R.; Muenter, M.; Baptista, M.; Miller, D.; Blancato, J.; Hardy, J.; Gwinn-Hardy, K. α-Synuclein Locus Triplication Causes Parkinson's Disease. *Science* **2003**, *302* (5646), 841.
(21) Tuttle, M. D.; Comellas, G.; Nieuwkoop, A. J.; Covell, D. J.; Berthold, D. A.; Kloepper, K. D.; Courtney, J. M.; Kim, J. K.; Barclay, A. M.; Kendall, A.; Wan, W.; Stubbs, G.; Schwieters, C. D.; Lee, V. M.; George, J. M.; Rienstra, C. M. Solid-state NMR structure of a pathogenic fibril of full-length human α-synuclein. *Nat. Struct. Mol. Biol.* **2016**, *23* (5), 409−415.
(22) Bousset, L.; Pieri, L.; Ruiz-Arlandis, G.; Gath, J.; Jensen, P. H.; Habenstein, B.; Madiona, K.; Olieric, V.; Bockmann, A.; Meier, B. H.; Melki, R. Structural and functional characterization of two alpha-synuclein strains. *Nat. Commun.* **2013**, *4*, 2575.
(23) Gath, J.; Bousset, L.; Habenstein, B.; Melki, R.; Meier, B. H.; Bockmann, A. Yet another polymorph of α-synuclein: solid-state sequential assignments. *Biomol. NMR Assignments* **2014**, *8* (2), 395−404.
(24) Heise, H.; Hoyer, W.; Becker, S.; Andronesi, O. C.; Riedel, D.; Baldus, M. Molecular-level secondary structure, polymorphism, and dynamics of full-length α-synuclein fibrils studied by solid-state NMR. *Proc. Natl. Acad. Sci. U.S.A.* **2005**, *102* (44), 15871−15876.
(25) Li, B.; Ge, P.; Murray, K. A.; Sheth, P.; Zhang, M.; Nair, G.; Sawaya, M. R.; Shin, W. S.; Boyer, D. R.; Ye, S.; Eisenberg, D. S.; Zhou, Z. H.; Jiang, L. Cryo-EM of full-length α-synuclein reveals fibril polymorphs with a common structural kernel. *Nat. Commun.* **2018**, *9* (1), 3609.
(26) Guerrero-Ferreira, R.; Taylor, N. M.; Arteni, A. A.; Kumari, P.; Mona, D.; Ringler, P.; Britschgi, M.; Lauer, M. E.; Makky, A.; Verasdonck, J.; Riek, R.; Melki, R.; Meier, B. H.; Böckmann, A.; Bousset, L.; Stahlberg, H. Two new polymorphic structures of human full-length alpha-synuclein fibrils solved by cryo-electron microscopy. *eLife* **2019**, *8*, No. e48907.
(27) Boyer, D. R.; Li, B.; Sun, C.; Fan, W.; Zhou, K.; Hughes, M. P.; Sawaya, M. R.; Jiang, L.; Eisenberg, D. S. The α-synuclein hereditary mutation E46K unlocks a more stable, pathogenic fibril structure. *Proc. Natl. Acad. Sci. U.S.A.* **2020**, *117* (7), 3592−3602.
(28) Boyer, D. R.; Li, B.; Sun, C.; Fan, W.; Sawaya, M. R.; Jiang, L.; Eisenberg, D. S. Structures of fibrils formed by α-synuclein hereditary disease mutant H50Q reveal new polymorphs. *Nat. Struct. Mol. Biol.* **2019**, *26* (11), 1044−1052.
(29) Yang, Y.; Garringer, H. J.; Shi, Y.; Lövestam, S.; Peak-Chew, S.; Zhang, X.; Kotecha, A.; Bacioglu, M.; Koto, A.; Takao, M.; Spillantini, M. G.; Ghetti, B.; Vidal, R.; Murzin, A. G.; Scheres, S. H. W.; Goedert, M. New SNCA mutation and structures of α-synuclein filaments from juvenile-onset synucleinopathy. *Acta Neuropathol.* **2023**, *145* (5), 561−572.
(30) Yang, Y.; Shi, Y.; Schweighauser, M.; Zhang, X.; Kotecha, A.; Murzin, A. G.; Garringer, H. J.; Cullinane, P. W.; Saito, Y.; Foroud, T.; Warner, T. T.; Hasegawa, K.; Vidal, R.; Murayama, S.; Revesz, T.; Ghetti, B.; Hasegawa, M.; Lashley, T.; Scheres, S. H. W.; Goedert, M. Structures of α-synuclein filaments from human brains with Lewy pathology. *Nature* **2022**, *610* (7933), 791−795.
(31) Schweighauser, M.; Shi, Y.; Tarutani, A.; Kametani, F.; Murzin, A. G.; Ghetti, B.; Matsubara, T.; Tomita, T.; Ando, T.; Hasegawa, K.; Murayama, S.; Yoshida, M.; Hasegawa, M.; Scheres, S. H.; Goedert, M. Structures of α-synuclein filaments from multiple system atrophy. *Nature* **2020**, *585* (7825), 464−469.
(32) Rockenstein, E.; Nuber, S.; Overk, C. R.; Ubhi, K.; Mante, M.; Patrick, C.; Adame, A.; Trejo-Morales, M.; Gerez, J.; Picotti, P.; Jensen, P. H.; Campioni, S.; Riek, R.; Winkler, J.; Gage, F. H.; Winner, B.; Masliah, E. Accumulation of oligomer-prone α-synuclein exacerbates synaptic and neuronal degeneration in vivo. *Brain* **2014**, *137* (5), 1496−1513.
(33) Cascella, R.; Chen, S. W.; Bigi, A.; Camino, J. D.; Xu, C. K.; Dobson, C. M.; Chiti, F.; Cremades, N.; Cecchi, C. The release of toxic oligomers from α-synuclein fibrils induces dysfunction in neuronal cells. *Nat. Commun.* **2021**, *12* (1), 1814.
(34) Ray, S.; Singh, N.; Kumar, R.; Patel, K.; Pandey, S.; Datta, D.; Mahato, J.; Panigrahi, R.; Navalkar, A.; Mehra, S.; Gadhe, L.; Chatterjee, D.; Sawner, A. S.; Maiti, S.; Bhatia, S.; Gerez, J. A.; Chowdhury, A.; Kumar, A.; Padinhateeri, R.; Riek, R.; Krishnamoorthy, G.; Maji, S. K. α-Synuclein aggregation nucleates through liquid-liquid phase separation. *Nat. Chem.* **2020**, *12* (8), 705−716.
(35) Xu, B.; Huang, S.; Liu, Y.; Wan, C.; Gu, Y. M.; Wang, D.; Yu, H. Manganese promotes α-synuclein amyloid aggregation through the induction of protein phase transition. *J. Biol. Chem.* **2022**, *298* (1), 101469.
(36) Xu, B.; Chen, J.; Liu, Y. Curcumin Interacts with α-Synuclein Condensates To Inhibit Amyloid Aggregation under Phase Separation. *ACS Omega* **2022**, *7* (34), 30281−30290.
(37) Piroska, L.; Fenyi, A.; Thomas, S.; Plamont, M. A.; Redeker, V.; Melki, R.; Gueroui, Z. α-Synuclein liquid condensates fuel fibrillar α-synuclein growth. *Sci. Adv.* **2023**, *9* (33), No. eadg5663.
(38) Hardenberg, M. C.; Sinnige, T.; Casford, S.; Dada, S. T.; Poudel, C.; Robinson, E. A.; Fuxreiter, M.; Kaminksi, C. F.; Kaminski Schierle, G. S.; Nollen, E. A. A.; Dobson, C. M.; Vendruscolo, M. Observation of an α-synuclein liquid droplet state and its maturation into Lewy body-like assemblies. *J. Mol. Cell Biol.* **2021**, *13* (4), 282−294.
(39) Harper, M.; Nudurupati, U.; Workman, R. J.; Lakoba, T. I.; Perez, N.; Nelson, D.; Ou, Y.; Punihaole, D. Toward determining amyloid fibril structures using experimental constraints from Raman spectroscopy. *J. Chem. Phys.* **2023**, *159* (22), 225101.
(40) Maiti, N. C.; Apetri, M. M.; Zagorski, M. G.; Carey, P. R.; Anderson, V. E. Raman Spectroscopic Characterization of Secondary Structure in Natively Unfolded Proteins: α-Synuclein. *J. Am. Chem. Soc.* **2004**, *126* (8), 2399−2408.
(41) Hauptmann, A.; Hoelzl, G.; Mueller, M.; Bechtold-Peters, K.; Loerting, T. Raman Marker Bands for Secondary Structure Changes of Frozen Therapeutic Monoclonal Antibody Formulations During Thawing. *J. Pharm. Sci.* **2023**, *112* (1), 51−60.
(42) Riek, R.; Eisenberg, D. S. The activities of amyloids from a structural perspective. *Nature* **2016**, *539* (7628), 227−235.
(43) Frey, L.; Ghosh, D.; Qureshi, B. M.; Rhyner, D.; Guerrero-Ferreira, R.; Pokharna, A.; Kwiatkowski, W.; Serdiuk, T.; Picotti, P.; Riek, R.; Greenwald, J. On the pH-dependence of α-synuclein amyloid polymorphism and the role of secondary nucleation in seed-based amyloid propagation. *eLife* **2023**, *12*, RP93562.
(44) Fusco, G.; De Simone, A.; Gopinath, T.; Vostrikov, V.; Vendruscolo, M.; Dobson, C. M.; Veglia, G. Direct observation of the three regions in α-synuclein that determine its membrane-bound behaviour. *Nat. Commun.* **2014**, *5*, 3827.
(45) Fusco, G.; De Simone, A.; Arosio, P.; Vendruscolo, M.; Veglia, G.; Dobson, C. M. Structural Ensembles of Membrane-bound α-Synuclein Reveal the Molecular Determinants of Synaptic Vesicle Affinity. *Sci. Rep.* **2016**, *6*, 27125.
(46) Cascella, R.; Perni, M.; Chen, S. W.; Fusco, G.; Cecchi, C.; Vendruscolo, M.; Chiti, F.; Dobson, C. M.; De Simone, A. Probing the Origin of the Toxicity of Oligomeric Aggregates of α-Synuclein with Antibodies. *ACS Chem. Biol.* **2019**, *14*, 1352−1362.

(47) Ikenoue, T.; Lee, Y. H.; Kardos, J.; Saiki, M.; Yagi, H.; Kawata, Y.; Goto, Y. Cold denaturation of α-synuclein amyloid fibrils. *Angew. Chem. Int. Ed.* **2014**, *53* (30), 7799−7804.
(48) van Gils, J. H. M.; van Dijk, E.; Peduzzo, A.; Hofmann, A.; Vettore, N.; Schützmann, M. P.; Groth, G.; Mouhib, H.; Otzen, D. E.; Buell, A. K.; Abeln, S. The hydrophobic effect characterises the thermodynamic signature of amyloid fibril growth. *PLoS Comput. Biol.* **2020**, *16* (5), No. e1007767.
(49) Hughes, M. P.; Sawaya, M. R.; Boyer, D. R.; Goldschmidt, L.; Rodriguez, J. A.; Cascio, D.; Chong, L.; Gonen, T.; Eisenberg, D. S. Atomic structures of low-complexity protein segments reveal kinked β sheets that assemble networks. *Science* **2018**, *359* (6376), 698−701.
(50) Rout, S. K.; Cadalbert, R.; Schroder, N.; Wang, J.; Zehnder, J.; Gampp, O.; Wiegand, T.; Guntert, P.; Klingler, D.; Kreutz, C.; Knorlein, A.; Hall, J.; Greenwald, J.; Riek, R. An Analysis of Nucleotide-Amyloid Interactions Reveals Selective Binding to Codon-Sized RNA. *J. Am. Chem. Soc.* **2023**, *145* (40), 21915−21924.
(51) Runfola, M.; De Simone, A.; Vendruscolo, M.; Dobson, C. M.; Fusco, G. The N-terminal Acetylation of α-Synuclein Changes the Affinity for Lipid Membranes but not the Structural Properties of the Bound State. *Sci. Rep.* **2020**, *10* (1), 204.
(52) Anand, K.; Pal, D.; Hilgenfeld, R. An overview on 2-methyl-2,4-pentanediol in crystallization and in crystals of biological macromolecules. *Acta Crystallogr., Sect. D: Biol. Crystallogr.* **2002**, *58* (10), 1722−1728.
(53) Dumetz, A. C.; Chockla, A. M.; Kaler, E. W.; Lenhoff, A. M. Comparative Effects of Salt, Organic, and Polymer Precipitants on Protein Phase Behavior and Implications for Vapor Diffusion. *Cryst. Growth Des.* **2009**, *9* (2), 682−691.
(54) Munishkina, L. A.; Henriques, J.; Uversky, V. N.; Fink, A. L. Role of Protein−Water Interactions and Electrostatics in α-Synuclein Fibril Formation. *Biochemistry* **2004**, *43* (11), 3289−3300.
(55) Lautenschlager, J.; Stephens, A. D.; Fusco, G.; Strohl, F.; Curry, N.; Zacharopoulou, M.; Michel, C. H.; Laine, R.; Nespovitaya, N.; Fantham, M.; Pinotsi, D.; Zago, W.; Fraser, P.; Tandon, A.; St George-Hyslop, P.; Rees, E.; Phillips, J. J.; De Simone, A.; Kaminski, C. F.; Schierle, G. S. K. C-terminal calcium binding of α-synuclein modulates synaptic vesicle interaction. *Nat. Commun.* **2018**, *9* (1), 712.
(56) Takegoshi, K.; Terao, T. dipolar recoupling under very fast magic-angle spinning using virtual pulses. *Solid State Nucl. Magn. Reson.* **1999**, *13* (4), 203−212.
(57) Camilloni, C.; De Simone, A.; Vranken, W. F.; Vendruscolo, M. Determination of secondary structure populations in disordered states of proteins using nuclear magnetic resonance chemical shifts. *Biochemistry* **2012**, *51* (11), 2224−2231.
(58) Berjanskii, M. V.; Wishart, D. S. The RCI server: rapid and accurate calculation of protein flexibility using chemical shifts. *Nucleic Acids Res.* **2007**, *35*, W531−W537.
(59) Zheng, S. Q.; Palovcak, E.; Armache, J. P.; Verba, K. A.; Cheng, Y.; Agard, D. A. MotionCor2: anisotropic correction of beam-induced motion for improved cryo-electron microscopy. *Nat. Methods* **2017**, *14* (4), 331−332.
(60) Rohou, A.; Grigorieff, N. CTFFIND4: Fast and accurate defocus estimation from electron micrographs. *J. Struct. Biol.* **2015**, *192* (2), 216−221.
(61) Zivanov, J.; Nakane, T.; Forsberg, B. O.; Kimanius, D.; Hagen, W. J.; Lindahl, E.; Scheres, S. H. New tools for automated high-resolution cryo-EM structure determination in RELION-3. *eLife* **2018**, *7*, No. e42166.
(62) Guerrero-Ferreira, R.; Taylor, N. M.; Mona, D.; Ringler, P.; Lauer, M. E.; Riek, R.; Britschgi, M.; Stahlberg, H. Cryo-EM structure of alpha-synuclein fibrils. *eLife* **2018**, *7*, No. e36402.
(63) Murshudov, G. N.; Skubák, P.; Lebedev, A. A.; Pannu, N. S.; Steiner, R. A.; Nicholls, R. A.; Winn, M. D.; Long, F.; Vagin, A. A. REFMAC5 for the refinement of macromolecular crystal structures. *Acta Crystallogr., Sect. D: Biol. Crystallogr.* **2011**, *67* (4), 355−367.
(64) Emsley, P.; Lohkamp, B.; Scott, W. G.; Cowtan, K. Features and development of Coot. *Acta Crystallogr., Sect. D: Biol. Crystallogr.* **2010**, *66* (4), 486−501.
(65) Burnley, T.; Palmer, C. M.; Winn, M. Recent developments in the CCP-EM software suite. *Acta Crystallogr., Sect. D: Struct. Biol.* **2017**, *73* (6), 469−477.
(66) Pettersen, E. F.; Goddard, T. D.; Huang, C. C.; Meng, E. C.; Couch, G. S.; Croll, T. I.; Morris, J. H.; Ferrin, T. E. UCSF ChimeraX: Structure visualization for researchers, educators, and developers. *Protein Sci.* **2021**, *30* (1), 70−82.
(67) Morris, K. L.; Serpell, L. C. X-ray fibre diffraction studies of amyloid fibrils. *Methods Mol. Biol.* **2012**, *849*, 121−135.
(68) Bodner, C. R.; Dobson, C. M.; Bax, A. Multiple Tight Phospholipid-Binding Modes of α-Synuclein Revealed by Solution NMR Spectroscopy. *J. Mol. Biol.* **2009**, *390* (4), 775−790.
(69) Bigi, A.; Loffredo, G.; Cascella, R.; Cecchi, C. Targeting Pathological Amyloid Aggregates with Conformation-Sensitive Antibodies. *Curr. Alzheimer Res.* **2020**, *17* (8), 722−734.
(70) Evangelisti, E.; Zampagni, M.; Cascella, R.; Becatti, M.; Fiorillo, C.; Caselli, A.; Bagnoli, S.; Nacmias, B.; Cecchi, C. Plasma membrane injury depends on bilayer lipid composition in Alzheimer's disease. *J. Alzheimer's Dis.* **2014**, *41* (1), 289−300.
(71) Candelise, N.; Schmitz, M.; Llorens, F.; Villar-Piqué, A.; Cramm, M.; Thom, T.; da Silva Correia, S. M.; da Cunha, J. E. G.; Möbius, W.; Outeiro, T. F.; Álvarez, V. G.; Banchelli, M.; D'Andrea, C.; de Angelis, M.; Zafar, S.; Rabano, A.; Matteini, P.; Zerr, I. Seeding variability of different alpha synuclein strains in synucleinopathies. *Ann. Neurol.* **2019**, *85* (5), 691−703.

https://doi.org/10.1021/jacs.3c14703
J. Am. Chem. Soc. 2024, 146, 10537−10549